On 3D Scanning Technologies for Respiratory Mask Design

Dmitry Nikolayevich Znamenskiy

Abstract Within the Philips Research project a handheld, 3D face scanner has been developed to address the needs of CPAP mask design for Philips Respironics business unit. The scanner is based on the structure light technology proposed in [10], which is claimed to be motion robust, i.e. in typical conditions with shaky hands and moving objects, the scanner delivers sub-millimetre accurate 3D face models, suitable for the CPAP mask design applications. In this article we derive an analytic expression for the accuracy of the structured light scanner, where the lateral and axial measurement errors as a function of the hardware parameters and the object position and velocity. The analytic formulas can contribute to better understanding the motion invariant structured light technology and creates a room for the scanner specifications.

Keywords Apnoea · 3D scanning · CPAP

1 Introduction

Apnea Philips makes respiratory masks for patients with Obstructive Sleep Apnoea syndrome (OSA). OSA is a sleep disorder when people frequently stop breathing during the night due to closure of the upper airway, so people partially wake up many times during the night, which causes continual sleepiness during the day and other health disorders, see [1]. Sleep studies [2] show that 6–7% of western population suffer from at least a mild form of apnoea, where almost 85 % of the cases remains undiagnosed and untreated. Male gender, age, overweight, low muscle tone and snoring can increase the likelihood of apnoea up to 40 %.

Mask Design Since 1980, sleep apnoea is effectively treated [3] (but not cured) by providing positive air pressure which prevents the upper airway from obstruction. The positive air pressure (CPAP or Bi-PAP) is generated by a pump and delivered by means of a tube and a facial mask to a patient. As the patient is expected to sleep with

D.N. Znamenskiy (✉)
Philips Research, HTC36, 5656AE, Eindhoven, Netherlands
e-mail: Dmitry.Znamenskiy@philips.com

B. Anderssen et al. (eds.), *The Role and Importance of Mathematics in Innovation*, Mathematics for Industry 25,
DOI 10.1007/978-981-10-0962-4_2

the mask every might, the mask should ultimately fit the patient's face. If mask does not fit the face, a patient can get red marks where the mask contact is to tense, or air leaks where the mask contact is too loose. The air leaks reduce the efficiency of the therapy and, if the mask is leaking towards an eye, it can cause an eye inflammation. About 40 % of the patients stop with the treatment, due of problems with the mask [4].

Studying the facial dimensions of the average apnoea patient is a critical task in the making of small lightweight masks which would perfectly fit the patient.

While it is possible to find the average facial dimensions in various anthropometric surveys, e.g. like [5], the manual anthropometric measurements are often inaccurate, see [7], and the majority of studies does not address the specific subgroup and ethnicities of the OSA population. Moreover, the knowledge of the average facial dimensions is often not sufficient, as not only dimensions but also the face shape significantly varies per population group.

3D Scanning with structured light The respiratory mask design can considerably benefit form 3D scanning surveys, like [6], which collect data over the complete facial surface. While the 3D scanning technologies already became almost a commodity, it is hardly possible to find a commercial 3D camera for fast, robust and mobile data collection: a lightweight handheld device with acquisition time of less than a second, motion robust yet giving sub-millimetre accurate measurements. It was expected that the sub-millimetre scanner accuracy being comparable with the amplitude of the skin defects will result in sufficiently accurate average faces for meaningful mask design. Thus within Philips Research a new 3D face scanning technology was proposed, see [10] which could potentially meet the required specifications. Among different scanning methods [8], the so-called *structured light* was chosen.

Structured light method is based on the projection of a known pattern with a projector on a scene, and capturing of the resulting image with a camera of the scene. The camera is laterally displaced with respect to projector on the distance called the *baseline*. Similar to a stereo-camera, the system works on the basis of disparity as the camera captures laterally displaced codes where the amount of displacement depends on the distance to the object, see Fig. 1. Further the required depth resolution was

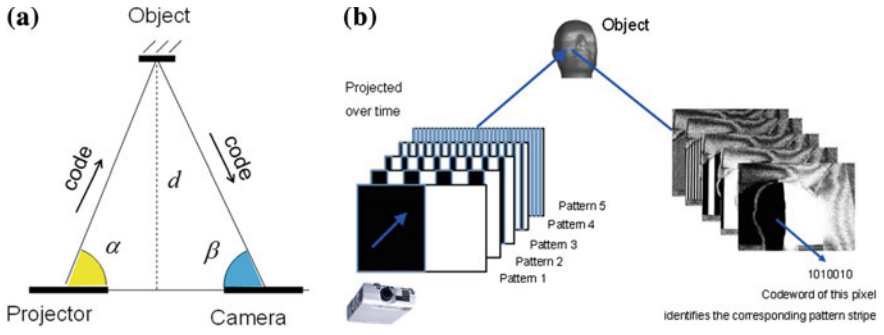

Fig. 1 **a** Triangulation principle, **b** a schematic of the structured light principle

gained using the sub-pixel accurate edge codes [9] and the motion invariance was achieved by alternating the polarity of the projected code images and using the edge addressing based on binary codes, where the position of decoded edges can be tracked from frame to frame, see [10]. The article is further structured as follows: In the next section we will present the main result. Then in Sect. 3 we will give an outline of the proof. Section 4 shows an application of the accuracy formulas to an example 3D scanner configuration. Section 5 describes embodiments of the structured light technology in Philips products. Appendix addresses the missing details.

2 Structured Light Accuracy

In order to better understand the potential of the technology and find the optimal scanner configuration, we invested time in derivation of an analytic expression for the accuracy of the scanner as a function of the hardware parameters and the object position and velocity. The scanner errors can be then translated to the accuracy of the average face computed over a collection of scans.

Consider the scanner and object optical system parameters: h-pixel size, Z_0—focusing distance, A—camera aperture size, f_c- camera focal length, N_r—sensor signal to noise ratio in percent of the camera dynamic range, F_s—frame rate, $C_{exp} \leq 1$—camera sensor image integration duty cycle, Z—distance to object, B—baseline between the camera and projector, V_x—relative lateral object velocity, V_z—relative object axial velocity, T_r—visible object texture intensity gradient in percent of dynamic range, see Fig. 2.

Proposition *The lateral scanner error E_X and the axial scanner error E_Z can be expressed as*

$$E_X \approx \frac{E \cdot Z}{f_c}, \qquad E_Z \approx \frac{E \cdot Z^2}{B \cdot f_c},$$

where E is the total system error which can be decomposed in the systematic and stochastic error

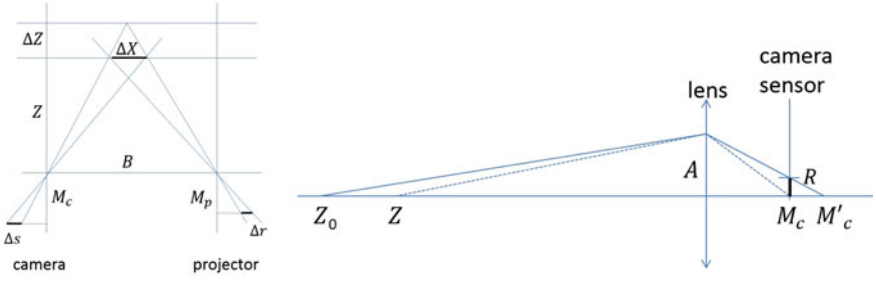

Fig. 2 Geometric parameters and camera blur

$$E = \bar{E} + E_n, \qquad \bar{E} \approx \frac{T_r \cdot V_X \cdot f_c}{2F_s \cdot Z} R, \qquad \bar{|E_n|} \leq \frac{N_r \cdot 3n}{2} R$$

where $n \sim N(0, 1)$ *is the Gaussian random variable and* R *is the system blur radius*

$$R = h + Af_c \frac{|Z - Z_0|}{Z \cdot Z_0} + \frac{|V_Z| \cdot B \cdot f_c \cdot C_{exp}}{F_s \cdot Z^2},$$

when the following two assumptions are satisfied:
(a) there are bounds on the relative lateral object speed V_X *and relative axial object speed* V_Z

$$|V_Z| \ll A \frac{|Z - Z_0| 2F_s \cdot Z}{Z_0 \cdot B}, \qquad |V_X| \ll A \frac{|Z - Z_0|}{Z_0} + \frac{|V_Z| \cdot B}{2F_s \cdot Z},$$

(b) the local texture gradient is not larger than the inverse of the system blur radius, i.e. $T_r \leq R^{-1}$.

3 Sketch of the Proof

The proof presented in this section is not rigorous/complete from the mathematical point of view, therefore we call it a 'sketch of the proof'. Below, we consider the projection and acquisition of the signal binary edge signal as the tracking of edges between the subsequent code frames is beyond the scope of the Proposition. The proof of the Proposition includes: (a) modelling of the optical system, (b) modelling of the camera signal, (c) modelling of the edge error and (d) application of the models.

Modelling of the optical system Below, we consider two Lemmas. The first one gives the relations between the real-world object localization error (object speed) versus the edge localization error (edge speed) on the camera sensor.

Lemma 1 *When* $\Delta Z \ll Z$ *and* $M_c \approx f_c$*, the object localization lateral error* E_X*, depth error* E_Z*, lateral object velocity* V_X *and axial object velocity* V_Z *are related to the edge localization error* E *and to the edge speed* v *on the camera sensor via the following equations:*

$$E_X \approx \frac{E \cdot Z}{f_c}, \qquad V_X \approx \frac{v_x \cdot Z}{f_c}, \qquad v_x \approx \frac{V_X \cdot f_c}{Z}, \qquad (a)$$

$$E_Z \approx \frac{E \cdot Z^2}{B \cdot f_c}, \qquad V_Z \approx \frac{v_z \cdot Z^2}{B \cdot f_c}, \qquad v_z \approx \frac{V_Z \cdot B \cdot f_c}{Z^2}, \qquad (b)$$

$$\Delta Z \approx \frac{\Delta r \cdot Z^2}{B \cdot M_p}. \qquad (c)$$

where v_x and v_z are the lateral edge speeds on the sensor caused respectively by the lateral and the axial object velocities.

The proof of lemma is given in appendix.

In the second lemma we give expression for the blur radius on the camera sensor as the function of the system parameters.

Lemma 2 *When $\Delta Z \ll Z$, $M_c \approx f_c$ and $f_c \ll Z_0$, the object appears blurred on the sensor with the blur radius*

$$R = h + Af_c \frac{|Z - Z_0|}{Z \cdot Z_0} + \frac{|V_Z| \cdot B \cdot f_c \cdot C_{exp}}{F_s \cdot Z^2},$$

Observe that the condition of the lemma is practically satisfied as for a typical small camera we have f_c equal to few mm, while Z and Z_0 are about tens of centimetres The proof of lemma is given in appendix.

Modelling of the edge signal Consider 1D camera sensor signal $I(s)$, $s \in \mathbb{R}$ which is sampled in the direction parallel to the baseline between the camera and the projector. We model $I(s)$ as the product of projected code signal $S(s)$ and the texture reflectivity $T(s)$, plus noise

$$I(s) = S(s) \cdot T(s) + \sigma \cdot n(s),$$

where $n(s) \sim N(0, 1)$ is the Gaussian random variable. Assume that the ideal edge position, at the absence of motion, texture crosstalk and noise is at $s = 0$ and that neighbouring pixel positions are at $s = h$, $s = -h$, where $2h$ is the distance between any two pixels on the sensor. At the absence of ambient light, object motion and sharply in the focus, the projected code signal can be modelled as

$$S(s) = \mathbb{1}(s \geq 0),$$

where $\mathbb{1}$ is the indicator function. In practical conditions, when the signal is superimposed over the ambient light S_0, and edge is acquired blurred with radius R, we model the signal $S(s)$ as

$$S(s) = a \cdot s + 0.5 + S_0, \qquad a = R^{-1}.$$

If object is moving in axial direction, the acquired signal appears displaced with speed v_z

$$S(s + v_z t) = a \cdot (s + v_z \cdot t) + 0.5 + S_0.$$

Note that the above model can be considered valid until

$$0 \leq S(s + v_z t) \leq 1. \tag{1}$$

We address the texture crosstalk effect with the simple linear model of the reflectivity

$$T(s) = c \cdot s + d,$$

where c, d are parameters such that $T(s) \in [0, 255]$. If an object is moving in lateral direction, the acquired texture appear displaced with speed v_x

$$T(s + v_x \cdot t) = c \cdot (s + v_x t) + d.$$

Combining the above edge and the camera model we have

$$\begin{aligned} I(s,t) &= S(s + v_z \cdot t) \cdot T(s + v_x \cdot t) + \sigma \cdot n(s). \\ &= \big(a \cdot (s + v_z \cdot t) + 0.5 + S_0\big) \cdot \big(c \cdot (s + v_x t) + d\big) + N_r d \cdot n(s), \end{aligned} \tag{2}$$

with $N_r = \sigma / d$.

Modelling of the edge error As we mentioned in the introduction we consider a coded light scheme where for every binary image pattern at time t we also project a negative of it at time $-t$. The edge signal in the positive-phase and negative-phase camera images can be modelled as

$$\begin{aligned} I_+(s,t) &= S(s - v_z \cdot t) \cdot T(s - v_x \cdot t) + \sigma \cdot n_+(s) \\ I_-(s,-t) &= S(-(s + v_z \cdot t)) \cdot T(s + v_x \cdot t) + \sigma \cdot n_-(s) \end{aligned} \tag{3}$$

where in the negative-phase camera images the edge signal is inverted while the texture signal stays the same. In order to cancel the effect of the unknown ambient light and minimize the influence of the local reflectivity on the exact position of the edge we normalize it as

$$I_n(s,t) = \frac{I_+(s,t) - I_-(s,-t)}{I_+(s,t) + I_-(s,-t)}. \tag{4}$$

The sub-pixel accurate observed edge position, i.e. edge error E, can be found by means of a linear interpolation of the normalized signal between the pixel positions $s = h$ and $s = -h$

$$E = h \cdot \frac{I_n(-h,t) + I_n(h,t)}{I_n(-h,t) - I_n(h,t)}, \tag{5}$$

see Fig. 3. Note, that the above approximation can be considered accurate until the estimated edge is located inside the pixel range

$$-h < E < h. \tag{6}$$

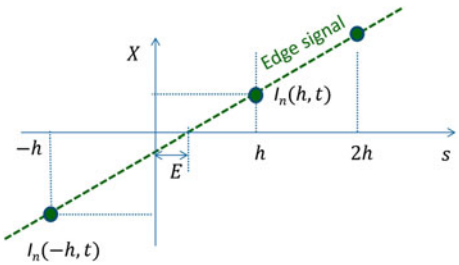

Fig. 3 Computation of the edge position E

Application of the models Observe that, due of Lemma 1, it is sufficient to prove under conditions of the Proposition that

$$\bar{E} \approx R\frac{c \cdot v_x \cdot t}{d}, \tag{7}$$

with $t = 1/(2F_s)$, and that

$$|E_n| = |E - \bar{E}| \leq R\frac{3N_r \cdot |n|}{2} \tag{8}$$

We prove first (7) and then (8). The first step towards this is the following lemma.

Lemma 3 *For E defined in (5) holds*

$$E = h \cdot \frac{I_+(-h,t) \cdot I_+(h,t) - I_-(-h,-t) \cdot I_-(h,-t)}{I_+(-h,t) \cdot I_-(h,-t) - I_-(-h,-t) \cdot I_+(h,t)}. \tag{9}$$

Proof The proof is quite straightforward. Substitute (4) in (5).

Let I_{pp}, I_{mp}, I_{pm} and I_{mm} denote $I_+(h,t), I_-(h,-t), I_+(-h,t)$ and $I_-(-h,-t)$ without noise, i.e.

$$\begin{aligned} I_{pp} &= S(h - v_z t)T(h - v_x t) \\ I_{pm} &= S(-h - v_z t)T(-h - v_x t) \\ I_{mp} &= S(-h - v_z t)T(h + v_x t) \\ I_{mm} &= S(h - v_z t)T(-h + v_x t) \end{aligned} \tag{10}$$

Below we define the systematic edge error which will be used to prove (7) and (8).

$$\bar{E} = h \cdot \frac{I_{pm}I_{pp} - I_{mm}I_{mp}}{I_{pm}I_{mp} - I_{mm}I_{pp}}. \tag{11}$$

Let us make some change of variables

$$\mu = v_z \cdot t, \qquad \nu = v_x \cdot t, \qquad \beta = d/c = T_r^{-1}.$$

The following lemma is then used to reduce $\bar{E}$

Lemma 4

$$(a)\quad I_{pm}I_{pp} - I_{mm}I_{mp} = 4d^2T_r\nu(1 - a^2h^2 - 2a\mu + a^2\mu^2)$$
$$(b)\quad I_{pm}I_{mp} - I_{mm}I_{pp} = h \cdot 4d^2\big(a - a^2\mu + T_r^2(\nu - ah^2 - 2a\mu\nu - a\nu^2 + a^2h^2(\mu + \nu) + a^2\mu^2\nu + a^2\mu\nu^2)\big) \tag{12}$$

Proof The proof is quite straightforward, but tediuos: use the suggested above change of variables and substitute (10) on the left-hand side of the lemma to get the expressions after simplification.

It follows from Lemma 4 that

$$\bar{E} = \frac{T_r\nu(1 - a^2h^2 - 2a\mu + a^2\mu^2)}{(a - a^2\mu + T_r^2(\nu - ah^2 - 2a\mu\nu - a\nu^2 + a^2h^2(\mu + \nu) + a^2\mu^2\nu + a^2\mu\nu^2)} \approx \frac{T_r\nu}{a} = R\frac{c \cdot v_x \cdot t}{d},$$

under assumptions of the Proposition which gives (7). In order to prove (8) we have to compare (9) and (11). The following Lemma compares respectively the nominators and denominators in (9) and (11).

Lemma 5 *Under assumptions of the Proposition we have*

$$\big(I_+(-h,t)\cdot I_+(h,t) - I_-(-h,-t)\cdot I_-(h,-t)\big) - \big(p_{pm}p_{pp} - p_{mm}p_{mp}\big) \approx 2d\sigma \cdot n_1,$$

and, similarly,

$$\big(I_+(-h,t)\cdot I_-(h,-t) - I_-(-h,-t)\cdot I_+(h,t)\big) - \big(p_{pm}p_{mp} - p_{mm}p_{pp}\big) \approx 2d\sigma \cdot n_2,$$

where n_1, n_2 are normal distributed random variables with variances at most 1.

The proof of Lemma 4 is given in the appendix. It follows then from Lemma 5 that

$$E \approx h\frac{4d^2T_r\nu + 2d\sigma \cdot n_1}{h \cdot 4d^2a + 2d\sigma \cdot n_2} = h\frac{2dT_r\nu + \sigma \cdot n_1}{h \cdot 2da + \sigma \cdot n_2}.$$

In order to proceed with proving (8) we need another lemma.

Lemma 6 *Let $n_1, n_2 \sim N(0,1)$ are normal distributed random variables. Under condition $n_1, n_2 \ll A, B$ and $A/B \le h$, there exist normal distributed random variable $n_3 \sim N(0,1)$ such that,*

$$\left|\frac{A + \sigma_1 \cdot n_1}{h \cdot B + \sigma_1 \cdot n_2} - \frac{A}{B}\right| \le \frac{3\sigma_1 \cdot |n_3|}{B}.$$

We apply Lemmas 4 and 6 with

$$A = 2dT_r v,$$

$$B = 2da,$$

to get (8):

$$|E_n| = |E - \bar{E}| \approx \left| h \cdot \frac{p_{pm}p_{pp} - p_{mm}p_{mp} + 2d\sigma \cdot n_1}{p_{pm}p_{mp} - p_{mm}p_{pp} + 2d\sigma \cdot n_2} - h \cdot \frac{p_{pm}p_{pp} - p_{mm}p_{mp}}{p_{pm}p_{mp} - p_{mm}p_{pp}} \right|$$

$$|E_n| \leq \frac{3\sigma \cdot |n_3|}{2d \cdot a} \approx R\frac{3N_r \cdot |n_3|}{2},$$

with $N_r = \sigma/d$, which completes the proof of the Proposition. □

4 Simulations

Consider, as example, a 3D scanner model with the following optical and system parameters. The camera sensor pixel size is 6×10^{-6} [m] which gives half of the distance between the pixels $h = 3 \times 10^{-6}$ [m]. The camera has the focal length $f_c = 0.008$ [m], F—number 2.5 and therefore the aperture $A = f_c/2.5 = 0.0032$ [m]. The camera is focused at distance $Z_0 = 0.4$ [m], and the active range of the scanner is $0.3\,[\text{m}] < Z < 0.7\,[\text{m}]$. The magnification of the camera $M_c = \frac{Z_0 \cdot f_c}{Z_0 - f_c} \approx f_c = 0.008$ [m]. Further we assume that the reflectivity change between the neighbouring pixels is 10 %. Hence $T_r/(2\text{h}) = 0.1$ and $T_r = 0.05/\text{h} \approx 1.7 \times 10^4$ [m]. The typical sensor SNR can be taken as $N_r = 1\,\%$ at the focusing distance $Z_0 = 0.4$ [m], and it grows as fourth power of distance to the object (a multiplication of the second power decay of projected intensity and second power decay of reflected intensity), which gives $N_r = (0.7/0.4)^4 1\,\% \approx 9.3\,\%$ at $Z = 0.7$ [m] and $N_r = (0.3/0.4)^4 1\,\% \approx 0.3\,\%$ at $Z = 0.3$ [m]. Take the baseline between the camera and projector $B = 0.07$ [m]. The camera frame rate is $F_s = 60\,[\text{s}^{-1}]$ and duty cycle 50 %, which gives the temporal image integration time of $120^{-1}\,[\text{s}^{-1}]$. Below we have applied the Proposition to make the level plot for the position error as a function of the lateral and axial object velocities. The set of first plots show the lateral and axial errors when the object is in focus at distance $Z_0 = 0.4$ [m]. One can see that the stochastic error variance is negligible (Fig. 4).

The second set of the plots shows the lateral and axial errors when the object is at distance $Z = 0.5$ [m]. The stochastic error variance for axial error is about millimetre and cannot be ignored anymore (Fig. 5).

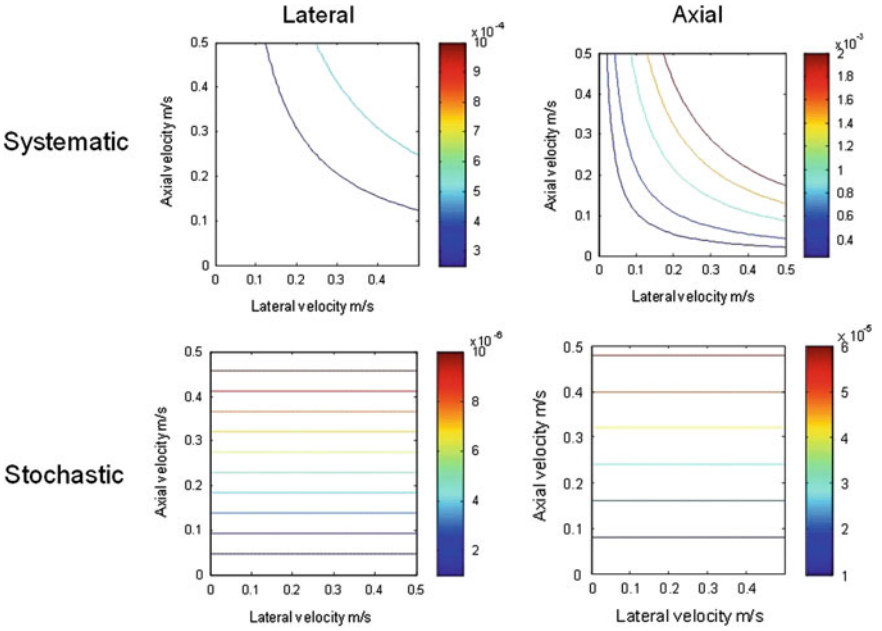

Fig. 4 Contour plots for scanning distance of 0.4 m

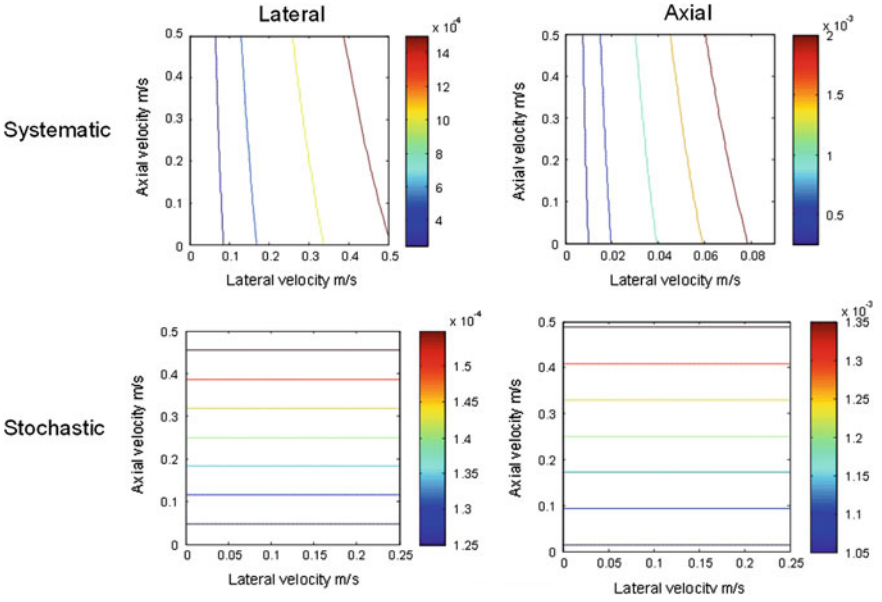

Fig. 5 Contour plots for scanning distance of 0.5 m

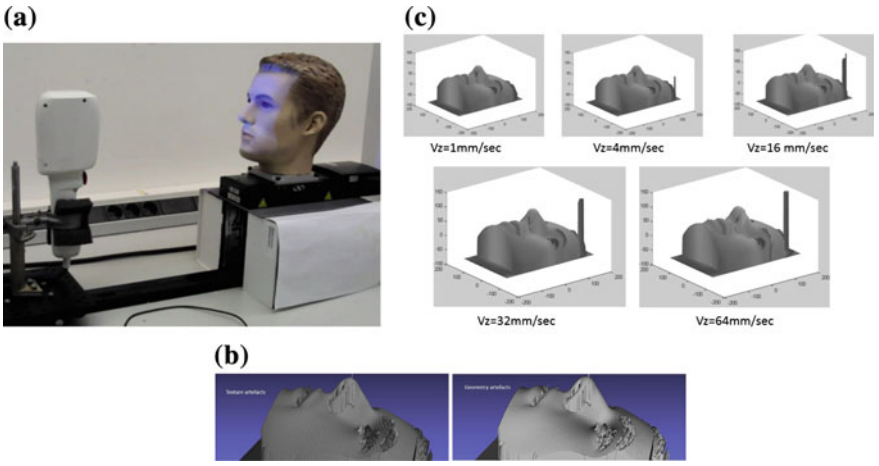

Fig. 6 **a** Scanner evaluation on the translation stage, **b** captured 3D image for different velocities, **c** artefacts at the maximal velocity

5 Realization in Products

On the practical side the new 3D scanning technologies were realized in a handheld 3D scanner Fig. 7a. The robustness of the scanner to the object motion was evaluated in a series of experiments where a manikin head was scanned while it was moving with certain velocity. The exact axial velocity was controlled by means of a translation stage, see Fig. 6. The 3D scans created with the scanner have sub-millimetre errors while the relative subject motion has the lateral and axial velocity of 5 and 20 cm/s respectively. Philips used 3D scanners to measure the OSA patients in Japan and design a special mask for Japanese OSA population, see Fig. 7b.

Acknowledgments The authors are grateful to Philips Respironics for providing a challenging topic of research, and to colleagues Ruud Vlutters and Karl van Bree who are co-authors of the motion invariant structured light principle [10].

Appendix

Proof of Lemma 1. Consider the left sketch on Fig. 2. From the similarity of triangles in the figure one can derive that

$$\frac{\Delta X}{Z} = \frac{\Delta s}{M_c} \tag{13}$$

$$\frac{\Delta Z}{\Delta X} = \frac{Z + \Delta Z}{B} \tag{14}$$

Fig. 7 **a** Philips internal 3D scanner, **b** a special version of Philips Wisp mask produced for Japanese market

The first one for $M_c \approx f_c$ implies

$$\Delta X = \frac{\Delta s \cdot Z}{M_c} \approx \frac{\Delta s \cdot Z}{f_c}, \tag{15}$$

and

$$\Delta s = \frac{\Delta X \cdot M_c}{Z} \approx \frac{X f_c}{Z} \tag{16}$$

Thus, if the object is displaced in the lateral direction we have point (a) of the Lemma:

The combination of the (14) and (15) implies

$$\Delta Z = \frac{\Delta s \cdot Z \cdot (Z + Z)}{B \cdot M_c} \tag{17}$$

If we assume that $\Delta Z \ll Z$, and $M_c \approx f_c$ we can approximate

$$\Delta Z \approx \frac{\Delta s \cdot Z^2}{B \cdot f_c}, \qquad \Delta s \approx \frac{\Delta Z \cdot B \cdot f_c}{Z^2}, \tag{18}$$

which implies points (b) and (c) of the Lemma. Thus, if the object is moving in the axial direction we have point (a) of the Lemma. The proof of point (c) can be obtained by flipping the camera and the projector sides. □

Proof of Lemma 2. We model the blur radius as the sum of the pixel blur, the optical blur and the motion blur.

$$R = R_h + R_o + R_m.$$

We assume the pixel blur equal to h, i.e. $R_h = h$. Consider first the optical blur. Suppose than the camera is focused at distance Z_0. Then we have from the lens equation

$$\frac{1}{Z_0} + \frac{1}{M_c} = \frac{1}{f_c}$$

Hence

$$M_c = \frac{Z_0 \cdot f_c}{Z_0 - f_c}.$$

If the object is located at distance Z, then the image is focused at distance

$$M_c^{'} = \frac{Z \cdot f_c}{Z - f_c}.$$

Then the object appears blurred on the sensor with the blur radius:

$$R_o = \frac{A}{M_c^{'}} |M_c^{'} - M_c| = A f_c \frac{|Z - Z_0|}{Z(Z_0 - f_c)} \approx A f_c \frac{|Z - Z_0|}{Z \cdot Z_0},$$

since $f_c \ll Z_0$. Consider the motion blur part. When the object is moving in the axial direction it causes the acquired edge move in laterally on the sensor, and the edge displacement R_m is equal to the absolute edge velocity $|v_z|$ times the exposure time T_{exp}:

$$R_m = v_z \cdot T_{exp} \approx \frac{|V_Z| \cdot B \cdot f_c \cdot C_{exp}}{Z^2 \cdot F_s},$$

where we apply Lemma 1, and where $T_{exp} = C_{exp}/F_s$ □

Proof of Lemma 5. It follows from the definitions of $I_+(h, t)$, $I_-(h, -t)$, $I_+(-h, t)$, $I_-(-h, -t)$ and I_{pp}, I_{mp}, I_{pm}, I_{mm}, and from the independence of $n_+(h)$, $n_+(-h)$, $n_-(h)n_-(-h)$ that

$$\begin{aligned}
&\big((I_+(-h, t) \cdot I_+(h, t) - I_-(-h, -t) \cdot I_-(h, -t)\big) - \big(I_{pm} I_{pp} - I_{mm} I_{mp}\big) \\
&= I_{pm}\sigma \cdot n_+(h) + I_{pp}\sigma \cdot n_+(-h) + I_{mm}\sigma \cdot n_-(h) - I_{mp}\sigma \cdot n_-(-h) \\
&= \sqrt{I_{pm}^2 + I_{pp}^2 + I_{mm}^2 + I_{mp}^2}\sigma \cdot n_1, \\
&\approx \sqrt{4a^2c^2R^2\beta^2}\sigma \cdot n_1 = 2d \cdot \sigma \cdot n_1,
\end{aligned}$$

for some $n_1 \sim N(0, 1)$. Similarly we get the second statement of the lemma. □

Proof of Lemma 6.

$$\left|\frac{A+\sigma_1\cdot n_1}{h\cdot B+\sigma_1\cdot n_2}-\frac{A}{B}\right|\approx\left|\frac{A}{B}\left(1+\frac{\sigma_1\cdot n_1}{A}\right)\left(1-\frac{\sigma_1\cdot n_2}{h\cdot B}\right)-\frac{A}{B}\right|$$

$$\approx\frac{A}{B}\left(\frac{\sigma_1\cdot n_1}{A}-\frac{\sigma_1\cdot n_2}{h\cdot B}\right)\leq\frac{2\sigma_1\cdot|n_3|}{B},$$

for some $n_3\sim N(0,1)$. □

References

1. Guilleminault, C., Tilkian, A., Dement, W.C.: The sleep apnea syndromes. Annu. Rev. Med. **27**, 465–484 (1976)
2. Young, T., Peppard, P.E., Gottlieb, D.J.: Epidemiology of obstructive sleep apnea: a population health perspective. Am. J. Respir. Crit. Care Med. **165**(9), 1217–1239 (2002)
3. Sullivan, C.E., Issa, F.G., Berthon-Jones, M., Eves, L.: Reversal of obstructive sleep apnoea by continuous positive airway pressure applied through the nares. Lancet **18**(1), 8225–8625 (1981)
4. Weigelt, L., Westbrook, P., Doshi, R.: Dissatisfaction with OSA management among CPAP rejecters and the role of the primary care physician. Sleep **33**, A159 (2010)
5. Yong J.W.: Head and Face Anthropometry of Adult U.S. Citizens, AD-A268 661 (1993). http://www.faa.gov/data_research/research/med_humanfacs/oamtechreports/1990s/media/am93-10.pdf
6. Zhuang Z., Bradtmiller B., Friess M.: A head and face anthropometry survey of U.S. respirator users, NIOSH NPPTL Anthrotech report, 28 May 2004. http://www.nap.edu/html/11815/Anthrotech_report.pdf
7. Farkas L.G.: Accuracy of anthropometric measurements: past, present, and future. Cleft Palate Craniofac J. **33**(1) 10–8; discussion 19–22 (1996)
8. Salvi, J., et al.: Pattern codification strategies in structured light systems. Pattern Recognit. **37**, 827–849 (2004)
9. Sato K.: Range imaging based on moving pattern light and spatio-temporal matched filter. In: Proceedings of the International Conference on Image Processing, 1996, vol. 1, pp. 33–36, 16–19 September 1996
10. Znamenskiy D.N., Vlutters R., van Bree K.C.: 3D Scanner using structured lighting, patent application US 20150204663, 23 July 2015

http://www.springer.com/978-981-10-0961-7

The Role and Importance of Mathematics in Innovation
Proceedings of the Forum "Math-for-Industry" 2015
Anderssen, B.; Broadbridge, P.; Fukumoto, Y.;
Kamiyama, N.; Mizoguchi, Y.; Polthier, K.; Saeki, O. (Eds.)
2017, XII, 176 p. 69 illus., 52 illus. in color., Hardcover
ISBN: 978-981-10-0961-7